ISSN: 2688-8645

Static and Dynamic Responses of a Composite Catenary Riser with Internal Gas–Liquid Two-Phase Flow

Xueping Chang, Wencheng Mu

School of Mechatronic Engineering, Southwest Petroleum University, Chengdu, Sichuan, 610500, China

Abstract

This study examines the static and vortex-induced vibration (VIV) responses of a composite catenary riser conveying internal gas–liquid two-phase flow under external ocean currents. A static model of the catenary riser incorporating pipe–seabed interaction is formulated based on the principle of minimum potential energy, and the governing equations are discretized and solved using a finite-difference scheme combined with the Newton–Raphson iterative method. For dynamics, a wake-oscillator model is coupled with the riser equations to predict combined in-line and cross-flow motions, while the internal two-phase flow is described using the Monette–Pettigrew slip model. The coupled system is solved with a finite-element formulation using Newmark–β time integration and a fourth-order Runge–Kutta scheme. Parametric studies quantify the effects of gas volume fraction and fiber orientation angle on the equilibrium configuration, internal forces, and vibration responses. Results show that increasing gas volume fraction reduces peak tension and bending moment in the touchdown region, whereas smaller layup angles improve the overall load state. In addition, higher gas volume fraction increases vibration amplitudes and shifts the response toward lower-order modes, while larger layup angles primarily induce downstream migration of the dominant mode.

Keywords

Composite Materials; Catenary Riser; Gas–liquid Two-phase Flow; Vortex-induced Vibration; Wake Oscillator Model.

1. Introduction

Owing to its simple configuration, the lack of a dedicated top-tension compensation system, and its strong adaptability to platform motions, the catenary riser has become a key piece of equipment in deepwater oil and gas production. As oil and gas development moves into deeper waters, conventional steel risers are increasingly unable to meet the combined demands of cost effectiveness and safety, due to their high self-weight, susceptibility to corrosion, and limited fatigue life. Composite materials offer substantial potential for offshore engineering applications thanks to their high specific strength and stiffness, excellent corrosion resistance, and strong tailoring capability. A composite catenary riser can significantly reduce self-weight and, consequently, the load demand on the host platform. Moreover, its mechanical performance can be tailored through laminate layup design, making it a promising direction for next-generation deepwater riser systems [1].

However, during service, composite catenary riser operate in a highly complex multi-field coupled environment. Internally, the conveyed gas–liquid two-phase flow can induce flow-excited vibrations and pressure fluctuations; externally, ocean currents and waves may trigger VIV. Meanwhile, the riser is also subjected to a range of quasi-static loads, including self-weight, buoyancy, top tension, and seabed constraints. In particular, the coupling between internal gas–

ISSN: 2688-8645

liquid two-phase flow and externally induced VIV may lead to large-amplitude oscillations, accelerated fatigue damage, and even structural failure, posing a serious threat to the long-term integrity and safe operation of the riser.

Regarding static modeling of catenary riser, Chatjigeorgiou and Mavrakos [2] developed a nonlinear static analysis approach based on catenary theory, providing a foundation for configuration prediction that accounts for large deformations and boundary conditions in deepwater applications. In terms of dynamic behavior, Sarpkaya [3] provided a comprehensive review of the physical mechanisms underlying VIV of circular cylinders, highlighting the critical role of fluid–structure interaction in predicting the vibration response. For vibration problems of composite cylindrical shell structures, Kardomateas et al. [4] developed an anisotropic laminated-shell theory, providing a theoretical framework for the dynamic modeling of composite risers. For numerical simulation of VIV, the wake-oscillator model proposed by Facchinetti et al. [5] represents the coupling between vortex shedding and structural motion via a nonlinear oscillator, and has been widely adopted to predict VIV responses of risers. With respect to the influence of internal gas–liquid two-phase flow, Monette and Pettigrew [6] developed a flow-induced instability model that accounts for interfacial slip effects, which substantially improves the accuracy of vibration predictions under two-phase flow conditions.

Researchers in China have also conducted extensive work in this area. Chang et al. [7] developed a bidirectional fluid–structure interaction model for composite risers conveying gas–liquid two-phase flow, and systematically investigated how internal-flow parameters affect the VIV response. Li et al. [8] examined the coupled cross-flow and in-line VIV responses of the catenary riser in a uniform current field. Xing et al. [9] focused on the VIV characteristics of catenary risers under two-phase internal flow, revealing how the gas void fraction governs the vibration modes and response amplitudes. In addition, Chen [10] analyzed VIV and fatigue damage in deepwater multiphase-flow risers, while Li Huajun et al. [11] reviewed a range of VIV suppression technologies for marine risers, providing useful guidance for engineering mitigation and protection. Tsukada and Morooka [12], and Yamamoto et al. [13], carried out systematic investigations of VIV responses of catenary riser from numerical and experimental perspectives, respectively, providing important validation data for model assessment.

Despite notable progress in understanding the static and dynamic behavior of catenary riser, much of the existing work still has several limitations. First, the material is often treated as isotropic or characterized by only a single property, which does not fully reflect the anisotropy and tailorability inherent to laminated composites. Second, relatively few studies simultaneously account for interfacial slip in gas–liquid internal flow, externally induced VIV, and the multi-field coupling introduced by nonlinear pipe–seabed contact. Third, the underlying role of fiber layup angle—one of the most critical design parameters for composite risers—has yet to be systematically clarified in both static and dynamic responses.

Accordingly, this paper develops a coupled static–dynamic model for catenary riser that simultaneously captures composite anisotropy, slip effects in internal gas–liquid two-phase flow, externally induced VIV, and elastic seabed restraint. The static equilibrium configuration is obtained from a minimum-potential-energy formulation solved using a finite-difference scheme, while the dynamic response is analyzed by coupling a wake-oscillator VIV model with a finite element formulation. On this basis, the influences of gas volume fraction and fiber orientation angle on the static configuration, internal force distribution, and vibration characteristics of the riser are systematically investigated, with the aim of providing theoretical support for structural design and safety assessment of composite catenary riser systems.

ISSN: 2688-8645

2. Static and Dynamic Modeling of a Composite Catenary Riser

2.1. Static Model

Consider a composite catenary riser as shown in Fig. 1. A global Cartesian coordinate system is defined with the origin *O* located at the sea surface directly above the seabed wellhead; the *x*-axis points horizontally toward the platform, the *z*-axis points vertically downward toward the seabed, and the *y*-axis is normal to the plane of the catenary riser. Under the combined effects of gravity, buoyancy, and seabed elastic reaction, the riser naturally hangs within the *x*-*z* plane. Assuming that the ambient current flows in the positive *X* direction, the drag and lift forces associated with VIV excite in-line motion in the *x*-*z* plane and cross-flow motion in the *Y* direction, respectively.

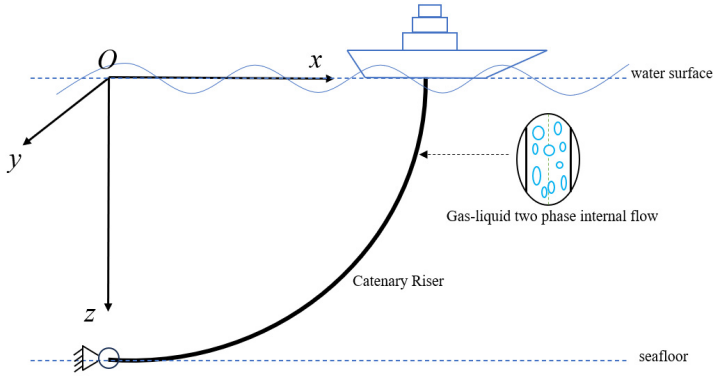

Fig 1. Schematic of the catenary riser.

The riser configuration can be characterized by the inclination angle with respect to the horizontal plane, from which the expressions for the *x*- and *z*-coordinates can be obtained as follows:

$$x(s) = \int_0^s \cos\theta(s')ds' \tag{1}$$

$$z(s) = -\int_s^L \sin\theta(s')ds' \tag{2}$$

the boundary conditions for the catenary riser are given by: $\theta_0 = 0^\circ$, $x(0) = 0$, $z(L) = 0$.

Based on the principle of minimum potential energy, the total potential energy U_{tot} of the catenary riser accounting for pipe seabed interaction can be expressed as:

$$\begin{aligned} U_{\text{tot}} = &\frac{1}{2}\int_0^L EI\left(\frac{d\theta}{ds}\right)^2 ds + \frac{1}{2}\int_0^{L_{\text{td}}} k_s[z(s)]^2 ds - \int_0^L wz(s)ds \\ &-\int_{L_{\text{td}}}^L \left[f_x x(s) + f_z z(s)\right]ds - P_x x(L) \end{aligned} \tag{3}$$

In Eq. (3), the first term represents the bending strain energy of the riser, where EI is the bending stiffness. The second term is the elastic strain energy associated with seabed support, with k_s denoting the seabed stiffness and L_{td} the length of the touchdown region. The third term corresponds to the gravitational potential energy, where w is the submerged weight per unit length. The fourth term is the potential associated with the hydrodynamic loading, in which f_x and f_z are the components of the distributed current load per unit length in the *X* and *Z* directions, respectively. The fifth term accounts for the work done by the horizontal component

ISSN: 2688-8645

of the top tension, where P_x denotes the prescribed horizontal tension. The static equilibrium configuration of the catenary riser is obtained by minimizing the total potential energy.

Using a finite-difference discretization, the riser is divided into *N* equal-length elements with element length $\Delta s = L / N$. The nodes are indexed as $i = 1, \cdots, N+1$, and the inclination angle at node i is denoted by θ_i. The total potential energy in discrete form can then be written as:

$$\begin{aligned} U_{\text{tot}} = \Delta s \sum_{i=1}^{N} \frac{EI}{2} \left(\frac{\theta_{i+1} - \theta_i}{\Delta s} \right)^2 + \sum_{i=1}^{N_{\text{td}}} \frac{k_s}{2} (z_i)^2 - \sum_{i=1}^{N} w z_i \\ - \sum_{i=N_{\text{td}}}^{N} \left(f_x^i x_i + f_z^i z_i \right) - P_x x_{N+1} \end{aligned} \tag{4}$$

where N_{td} is the number of nodes in the touchdown region, $z_i = \sum_{k=i}^{N} \Delta s \sin\theta_k$, $x_i = \sum_{k=1}^{i} \Delta s \cos\theta_k$.

Static equilibrium requires that the partial derivative of the total potential energy with respect to the inclination angle at each node θ_i vanish,

$$\frac{\partial U_{\text{tot}}}{\partial \theta_i} = 0, \quad i = 2, \ldots, N \tag{5}$$

Substituting Eq. (4) into the above condition yields the following system of finite-difference equations:

$$\begin{aligned} &\frac{EI}{\Delta s}(-\theta_{i-1} + 2\theta_i - \theta_{i+1}) + \sum_{j=1}^{i} k_s z_j \Delta s \cos\theta_i + \sum_{j=i}^{N} (f_z^j + w_s) \Delta s \cos\theta_i \\ &- \sum_{j=i}^{N} f_x^j \Delta s \sin\theta_i - P_0(-\Delta s \sin\theta_i) = 0, \quad i = 2, \ldots, N \end{aligned} \tag{6}$$

The discrete nonlinear system in Eq. (6) is solved iteratively using the Newton–Raphson method. At each iteration, the nodal inclination angles are updated by evaluating the residual vector and the Jacobian matrix until convergence is achieved and the equilibrium configuration is obtained. Once the riser shape is determined, the corresponding internal force distribution along the catenary can be further calculated.

2.2. Dynamic Model

Accounting for the effects of gravity, buoyancy, and initial tension, the governing dynamic equation for the composite catenary riser conveying gas–liquid two-phase flow can be written as [7]:

$$\begin{aligned} &a_{22} \frac{\partial^4 u}{\partial s^4} + a_{23} \frac{\partial^4 v}{\partial s^4} + (m_p + m_a + m_l + m_g) \frac{\partial^2 u}{\partial t^2} + (c + c') \frac{\partial u}{\partial t} \\ &+ (2m_l U_l + 2m_g U_g) \frac{\partial^2 u}{\partial t \partial s} + (m_l U_l^2 + m_g U_g^2) \frac{\partial^2 u}{\partial s^2} - \frac{\partial}{\partial s} \left(T_e \frac{\partial u}{\partial s} \right) = F_D, \end{aligned} \tag{7a}$$

$$\begin{aligned} &a_{33} \frac{\partial^4 v}{\partial s^4} + a_{32} \frac{\partial^4 u}{\partial s^4} + (m_p + m_a + m_l + m_g) \frac{\partial^2 v}{\partial t^2} + (c + c') \frac{\partial v}{\partial t} \\ &+ (2m_l U_l + 2m_g U_g) \frac{\partial^2 v}{\partial t \partial s} + (m_l U_l^2 + m_g U_g^2) \frac{\partial^2 v}{\partial s^2} - \frac{\partial}{\partial s} \left(T_e \frac{\partial v}{\partial s} \right) = F_L. \end{aligned} \tag{7b}$$

Here, u and v denote the in-line and cross-flow displacements, respectively. a_{22}, a_{33}, and a_{23} (a_{32}) are the in-line bending stiffness, cross-flow bending stiffness, and the coupled bending stiffness, respectively, whose formulations follow Librescu. m_p, m_a, m_l, and m_g represent the

ISSN: 2688-8645

structural mass per unit length, added mass, liquid-phase internal-flow mass, and gas-phase internal-flow mass per unit length, respectively. U_l and U_g are the mean velocities of the internal liquid and gas phases. T_e is the axial tension in the catenary riser, which can be obtained from the computed static configuration. c and c' are the structural and fluid damping coefficients, respectively, with $c = 2m\omega\varsigma$ and $c' = \gamma\Omega_f \rho D^2$; Ω_f is the vortex-shedding angular frequency $\Omega_f = 2\pi StU_0 / D$, and γ is the viscous damping coefficient $\gamma = C_{D0} / 4\pi St$. Finally, F_D and F_L are the hydrodynamic forces in the in-line and cross-flow directions, respectively.

VIV of marine risers is a self-excited oscillation driven by vortex shedding. Facchinetti [5] employed a van der Pol wake-oscillator model to represent the fluctuating lift and drag associated with vortex shedding from a circular cylinder. In this study, an acceleration-coupled van der Pol equation is adopted to describe the unsteady wake excitation acting on the riser due to vortex shedding:

$$\frac{\partial^2 p}{\partial t^2} + 2\varepsilon_u \Omega_f (p^2 - 1)\frac{\partial p}{\partial t} + (2\Omega_f)^2 p = \frac{A_u}{D}\frac{\partial^2 u}{\partial t^2}, \tag{8a}$$

$$\frac{\partial^2 q}{\partial t^2} + \varepsilon_v \Omega_f (q^2 - 1)\frac{\partial q}{\partial t} + \Omega_f^2 q = \frac{A_v}{D}\frac{\partial^2 v}{\partial t^2}. \tag{8b}$$

Here, p and q are the wake-oscillator variables associated with fluctuating drag and lift, respectively. A_u and A_v are the coupling coefficients between the wake and the structural acceleration, while ε_u and ε_v are the van der Pol damping parameters. These four quantities are empirical coefficients calibrated from experiments; the values adopted in this work are $A_u = 48$, $A_v = 12$, $\varepsilon_u = 1.2$, and $\varepsilon_v = 0.3$.

Based on the Morison equation, the expressions for the VIV-induced drag force F_D and lift force F_L acting on the riser can be written as:

$$F_D = \frac{1}{2}\rho_w D C_D U_0 \sqrt{\left(U_0 - \frac{\partial u}{\partial t}\right)^2 + \left(\frac{\partial v}{\partial t}\right)^2}, \tag{9a}$$

$$F_L = \frac{1}{2}\rho_w D C_L \left(U_0 - \frac{\partial u}{\partial t}\right)^2. \tag{9b}$$

Here, $C_D = C_{D0}\frac{q}{2}$ and $C_L = C_{L0}\frac{p}{2}$ are the drag and lift coefficients, while C_{D0} and C_{L0} denote the drag and lift coefficients of a stationary circular cylinder. Following the parameter selection in Ref. [10], the coefficients used in this study are $C_{D0} = 0.4$ and $C_{L0} = 0.3$. ρ_w is the density of the external fluid (seawater), and D is the outer diameter of the riser.

The gas–liquid two-phase flow model adopted in this paper follows the Monette–Pettigrew formulation [6]. Monette and Pettigrew [6] introduced a slip factor expressed as a function of void fraction to predict the relative slip between the gas and liquid phases in two-phase flow. They further validated the proposed model experimentally, showing that its predictions of the critical flow velocity and critical frequency agree much better with measurements than those from the homogeneous model ($K = 1$) and the Chisholm model K_c. The void fraction α, gas volume fraction ε_g, and velocity slip factor K are given by:

$$\alpha = \frac{C_g}{C_g + C_l}, \varepsilon_g = \frac{Q_g}{Q_g + Q_l}, K = \frac{U_g}{U_l}. \tag{10}$$

ISSN: 2688-8645

Here, C_g and C_l denote the volumes of the gas and liquid phases, respectively, while Q_g and Q_l are the corresponding volumetric flow rates. The slip factor introduced by Monette and Pettigrew is expressed as:

$$K = \frac{\alpha}{1-\alpha} = \sqrt{\frac{\varepsilon_g}{1-\varepsilon_g}}. \tag{11}$$

Substituting the slip-factor relation in Eq. (11) into Eq. (10) yields the expressions for the gas-phase mass per unit length m_g, the liquid-phase mass per unit length m_l, and the gas-phase flow velocity U_g appearing in the governing equations of motion Eq. (7):

$$U_g = U_l \cdot \sqrt{\frac{\varepsilon_g}{1-\varepsilon_g}}, \tag{12a}$$

$$m_l = \rho_l A_{\text{in}} \cdot \frac{1}{\sqrt{\frac{\varepsilon_g}{1-\varepsilon_g}}+1}, \tag{12b}$$

$$m_g = \rho_g A_{\text{in}} \cdot \frac{\sqrt{\frac{\varepsilon_g}{1-\varepsilon_g}}}{\sqrt{\frac{\varepsilon_g}{1-\varepsilon_g}}+1}. \tag{12c}$$

2.3. Numerical Solution Procedure.

2.3.1. Static Configuration Solution

To solve the static governing equations in Eq. (6) for the catenary riser, the Newton–Raphson iterative method is employed. The classical catenary solution neglecting bending stiffness is taken as the initial guess for the iteration.

$$z(x) = \frac{P_0}{w}\left[\cosh\left(\frac{w}{P_0}x\right)-1\right] \tag{13}$$

Differentiating Eq. (13) yields the corresponding expression for the inclination-angle distribution:

$$\theta(x) = \arctan\left[\sinh\left(\frac{w}{P_0}x\right)\right] \tag{14}$$

This further leads to the inclination-angle distribution as a function of arc length:

$$\theta(s) = \arctan\left(\frac{w}{P_0}s\right) \tag{15}$$

Since the actual riser length (L) is greater than the catenary length associated with the initial solution, a length-increment strategy is adopted to enhance numerical stability by gradually increasing the riser length. After each length increment, the residuals are evaluated using Eq. (6), and the inclination angles are updated through corrections obtained from the Jacobian matrix; the residuals are then recomputed iteratively until convergence. The Jacobian matrix is given by:

ISSN: 2688-8645

$$J_{ij} = \frac{EI}{\Delta s}(\delta_{i-1,j} - 2\delta_{ij} + \delta_{i+1,j}) - k_s \Delta s^2 \cos^2\theta_i \cdot \delta_{ij} \cdot H(-h_w - z_i) + P_0 \Delta s \cos\theta_i \cdot \delta_{ij} \tag{16}$$

where δ_{ij} is the Kronecker delta and $H(x)$ denotes the Heaviside step function.

2.3.2. Dynamic Response Solution

The equations of motion in Eq. (7) are solved using the finite element method. The static geometric and mechanical quantities obtained from the catenary analysis are used as inputs: the effective axial tension distribution along the riser is introduced as the tension term in the governing equations, and the computed static configuration is taken as the initial configuration. Accordingly, the dynamic displacement is defined as an incremental displacement superimposed on the static equilibrium shape.

The riser is discretized into N elements using cubic Hermite interpolation functions (with N chosen to be the same as that used in the static discretization to facilitate evaluation of the internal-force terms). The in-line and cross-flow displacements of the catenary riser can then be expressed as:

$$\begin{bmatrix} u(s) \\ v(s) \end{bmatrix} = \mathbf{N}(s)\mathbf{d}^{\mathbf{e}} \tag{17}$$

where d^e is the nodal displacement vector (matrix).

$$\mathbf{d}^{\mathbf{e}} = [u_1, v_1, \theta_{u1}, \theta_{v1}, u_2, v_2, \theta_{u2}, \theta_{v2}]^T \tag{18}$$

where $N(s)$ is the shape-function matrix.

$$\mathbf{N}(\xi) = \begin{bmatrix} N_1(\xi) & 0 & N_2(\xi) & 0 & N_3(\xi) & 0 & N_4(\xi) & 0 \\ 0 & N_1(\xi) & 0 & N_2(\xi) & 0 & N_3(\xi) & 0 & N_4(\xi) \end{bmatrix} \tag{19}$$

where

$$\begin{aligned} N_1(\xi) &= 1 - 3\xi^2 + 2\xi^3, \\ N_2(\xi) &= L_e(\xi - 2\xi^2 + \xi^3), \\ N_3(\xi) &= 3\xi^2 - 2\xi^3, \\ N_4(\xi) &= L_e(-\xi^2 + \xi^3). \end{aligned} \tag{20}$$

Using the displacement approximation in Eq. (17) and the Galerkin weighted-residual method, the governing vibration equations in Eq. (7) are transformed into the finite element form:

$$\mathbf{M}\ddot{\mathbf{D}} + \mathbf{C}\dot{\mathbf{D}} + \mathbf{K}\mathbf{D} = \mathbf{F} \tag{21}$$

Based on the coordinates and inclination angles obtained from the static catenary solution, the riser vibration equations are integrated using the Newmark–β method, while the wake-oscillator equations are solved using a fourth-order Runge–Kutta scheme. The computed in-line and cross-flow displacements in the local frame are then transformed using the catenary inclination angle, yielding the three-dimensional vibration response of the riser under the combined effects of internal gas–liquid two-phase flow and external current loading.

ISSN: 2688-8645

3. Numerical Results and Discussion

3.1. Model Validation

To validate the accuracy of the proposed static catenary model, the numerical predictions are compared with the experimental results reported by Liu Depeng [14]. The model parameters used for the validation are listed in Table 1.

Table 1. Parameters used for validation of the static catenary riser model.

Parameter	Value	Unit
Total riser length	1260	m
Water depth	900	m
Riser mass per unit length	189.1	kg/m
Gas-phase density	0.675	kg/m^3
Liquid-phase density	790	kg/m^3

The tension and bending moment of the catenary riser are computed for different riser-length cases, and the predictions are compared with those from Liu Depeng's model. The comparison is shown in Fig. 2. The present model shows good agreement with the results reported by Liu Depeng in terms of both tension and bending moment. As shown in Fig. 2(a), the axial tension increases monotonically with riser length, with a noticeably steeper rise in the region closer to the platform (after approximately 0.25 km). This trend is consistent with the underlying mechanics of a catenary system: the combined effects of gravity and hydrodynamic loading lead to a progressive accumulation of suspended weight along the riser, resulting in a continual increase in axial tension. Fig. 2(b) illustrates the variation of bending moment along the riser. The bending moment increases sharply in the near-seabed region (approximately 0-0.25 km), reaches a peak there, and then gradually decreases along the remaining length. The increase in bending moment can be attributed to the large curvature deformation experienced in the seabed-contact region. The contact constraint imposed by the seabed stiffness intensifies bending, whereas once the riser transitions into the free-hanging segment, the bending moment decreases progressively.

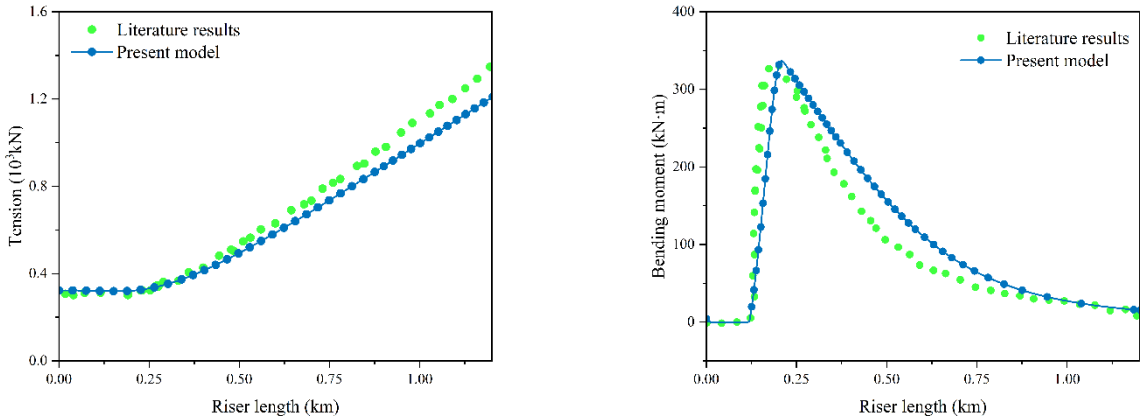

(a) Static tension (b) Static bending moment

Fig 2. Axial tension and bending moment distributions of the catenary riser

To validate the accuracy of the proposed dynamic catenary riser model, the numerical results are compared with the experimental data reported by Yamamoto [13] and Liu [15]. The model parameters used for the validation are given in Table 2.

ISSN: 2688-8645

Table 2. Parameters used for validation of the dynamic catenary riser model.

Parameter	Value	Unit	Parameter	Value	Unit
Total riser length	120	m	Seawater density	997	Kg/m^3
Top tension	200	kN	Young's modulus	210	GPa
Structural damping ratio	0.02	-	Outer diameter	0.25	m
Riser material density	7700	Kg/m^3	Wall thickness	0.0192	m

The dynamic catenary-riser model developed in this study is further assessed by comparing its predictions under different riser-length cases with the results reported by Yamamoto [13] and Liu [15], as shown in Fig. 3. The present results exhibit essentially the same trend in the dimensionless vibration amplitude as the literature data as the riser length varies. Specifically, the vibration amplitude increases with riser length initially and then levels off or decreases slightly, indicating that the proposed model captures the overall dynamic response characteristics of the catenary riser subjected to flow-induced vibration with good fidelity. Over most of the considered riser-length range, the present predictions agree well with those reported by Yamamoto and Liu, and the three curves nearly coincide for longer risers. This close agreement indicates that the proposed model achieves high accuracy in predicting the vibration response of long catenary riser.

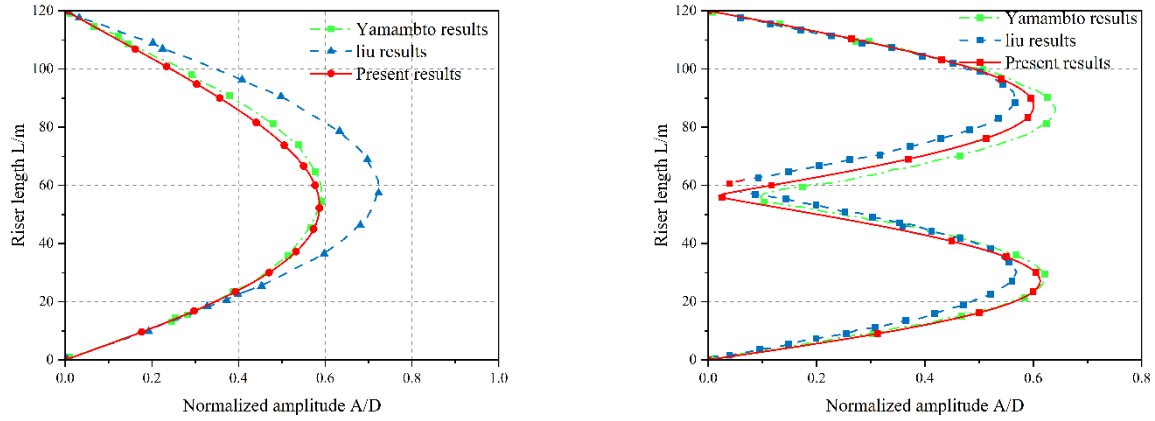

(a) External current velocity: 0.23 m/s (b) External current velocity: 0.38 m/s

Fig 3. Maximum cross-flow vibration amplitude of the catenary riser under different external current velocities.

3.2. Static Configuration and Internal Force Analysis of the Catenary Riser

Table 3. Baseline parameters of the composite catenary riser.

Parameter	Value	Unit	Parameter	Value	Unit
Riser length	300	m	Transverse Young's modulus	137	GPa
Water depth	200	m	Longitudinal Young's modulus	9	GPa
Riser density	1601	kg/m^3	Shear modulus	7.1	GPa
Top tension	100	kN	Poisson's ratio	0.3	-
Seawater density	1025	kg/m^3	Seabed stiffness	4	kN/m^2
Liquid-phase density	880	kg/m^3	External current velocity	0.38	m/s
Gas-phase density	1.293	kg/m^3	Liquid-phase velocity	1	m/s

Following the parameter settings for composite risers reported in Ref. [7], the baseline parameters used in the numerical simulations are summarized in Table 3. In addition, the thickness of each composite ply is 2 mm, and the laminate consists of 10 plies with a fiber

ISSN: 2688-8645

orientation sequence of $\pm 60^{\circ}$. Fig.3 presents the static configuration and internal force distributions of the composite catenary riser for different gas volume fractions ε_g (0.1, 0.3, 0.6, and 0.9). The influence of on the static performance is elucidated in terms of the spatial profile, axial tension distribution, bending-moment response, and shear-force distribution.

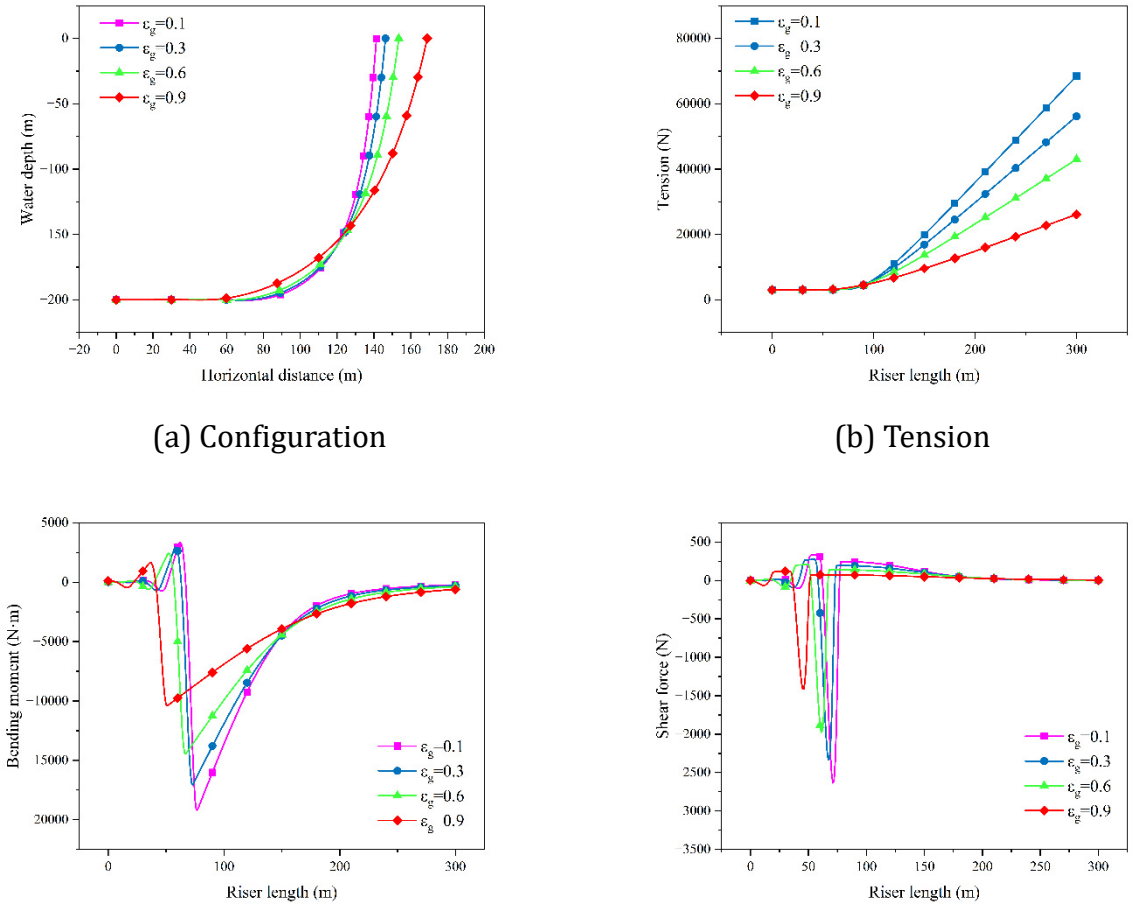

(a) Configuration (b) Tension

(c) Bending moment (d) Shear force

Fig 4. Static configuration and internal force distributions of the composite catenary riser for different gas volume fractions.

Fig. 4(a) shows the configuration variations of the composite catenary riser for different gas volume fractions. As ε_g increases from 0.1 to 0.9, the length of the touchdown segment decreases, the curvature near the touchdown point is reduced, and the overall profile becomes smoother. Meanwhile, the horizontal span of the riser increases. Fig. 4(b) presents the axial tension distribution along the composite catenary riser. In the touchdown region, the tension remains relatively low, at approximately 3000 N. As the arc length increases, the tension rises progressively, and the growth is most pronounced for the lower gas volume fraction ($\varepsilon_g = 0.1$). Specifically, when ($\varepsilon_g = 0.9$), the tension increases from about 3000 N to 26,145.01 N, whereas for ($\varepsilon_g = 0.1$), it increases from about 3000 N to 68,511.14 N. Fig. 4(c) shows the bending-moment distribution along the composite catenary riser. The maximum bending moment occurs near the touchdown point; within the riser–seabed contact region, the bending moment reaches its peak due to pronounced curvature variations and the associated boundary

ISSN: 2688-8645

constraints. As ε_g increases from 0.1 to 0.9, the touchdown region becomes shorter; consequently, the location of the peak bending moment shifts upstream (toward smaller arc length), and the peak value decreases accordingly. For (ε_g = 0.1, 0.3, 0.6, 0.9), the corresponding peak bending moments are 19,186.4, 17,067.3, 14,448.9, and 10,400.2, respectively. Fig. 4(d) shows the shear-force distribution along the riser and exhibits a similar pattern to that of the bending moment. The peak shear forces for(ε_g = 0.1, 0.3, 0.6, 0.9) are 2,635.6, 2,329.0, 1,978.9, and 1,411.4, respectively. These results demonstrate that the gas volume fraction has a pronounced influence on both the static configuration and internal forces of the composite catenary riser. Increasing ε_g can effectively improve the static load state, reducing the tension, bending moment, and shear force in critical regions.

Fig. 5 presents the static configuration and internal force distributions of the composite catenary riser for different fiber orientation angles θ (30°, 45°, 60°, 75°). The influence of θ on the static performance is examined in terms of the spatial profile, axial tension distribution, bending-moment response, and shear-force distribution.

Fig. 5(a) shows the configuration variations of the composite catenary riser for different fiber orientation angles. As θ increases from 30° to 75°, the length of the touchdown segment decreases, the curvature near the touchdown point is reduced, and the overall profile becomes smoother. Meanwhile, the horizontal span of the riser increases. Fig. 5(b) presents the axial tension distribution along the composite catenary riser. In the touchdown region, the tension remains relatively low, at approximately 3000N. As the arc length increases, the tension rises gradually. The tension profiles for different fiber orientation angles differ mainly in the vicinity of the touchdown point, whereas only minor differences are observed near the top end. Specifically, when ($\theta = 30^\circ$), the tension increases from about 3000 N to 42,990.2 N, while for ($\theta = 75^\circ$), it increases from about 3000 N to 43,070.7 N. Fig. 5(c) shows the bending-moment distribution along the composite catenary riser. The maximum bending moment occurs near the touchdown point; within the riser–seabed contact region, the bending moment reaches a peak due to curvature variations and boundary constraints. As θ increases from 30° to 75°, the touchdown region becomes shorter, and the location of the peak bending moment shifts upstream (toward smaller arc length), while the peak value increases. For θ=(30°, 45°, 60°, 75°), the corresponding peak bending moments are 5,666.9, 8,433.8, 14,448.9, and 22,159.2, respectively. Fig. 5(d) shows the shear-force distribution along the composite catenary riser and exhibits a trend similar to that of the bending moment. For θ=(30°, 45°, 60°, 75°), the corresponding peak shear forces are 1,272.7, 1,525.7, 1,978.9, and 2,387.7, respectively. These results indicate that the fiber orientation angle has a pronounced influence on both the static configuration and internal forces of the composite catenary riser. In contrast, increasing the gas volume fraction can effectively improve the static load state by reducing the tension, bending moment, and shear force in critical regions. The fiber orientation angle significantly influences the static equilibrium shape and internal force distribution of the composite riser by modifying the coupling between its axial and bending stiffness. Smaller layup angles ($\theta = 30^\circ$) are beneficial for improving the overall load state and reducing peak tension and bending moment in critical regions, whereas larger layup angles ($\theta = 75^\circ$) result in a deeper sag, increased local curvature, and higher bending moments, which may aggravate fatigue damage in the touchdown region.

ISSN: 2688-8645

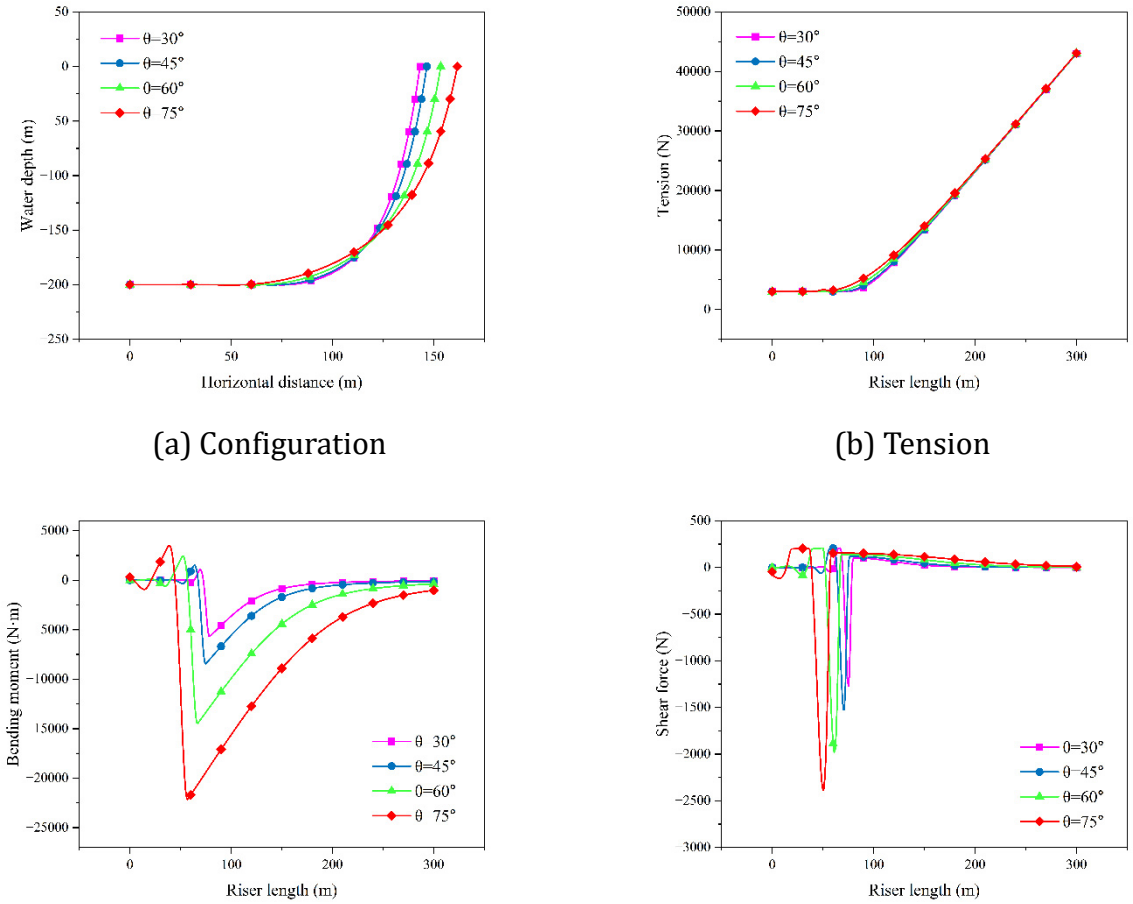

(a) Configuration (b) Tension

(c) Bending moment (d) Shear force

Fig 5. Static configuration and internal force distributions of the composite catenary riser for different fiber orientation angles.

3.3. Vibration Response of the Catenary Riser

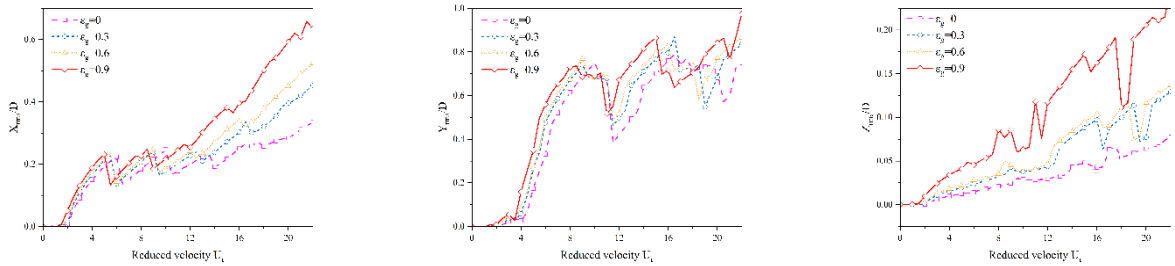

(a) *X* direction (b) *Y* direction (c) *Z* direction

Fig 6. Variation of the maximum RMS displacement with reduced velocity for different gas volume fractions.

With the operating water depth set to 250 m and all other parameters taken from Table 3. Fig. 6 shows the variation of the maximum root-mean-square (RMS) displacements in the *X*, *Y*, and *Z* degrees of freedom with reduced velocity for gas volume fractions of 0, 0.3, 0.6, and 0.9, respectively. As shown in Fig. 7, the variation of the maximum RMS displacement with reduced velocity is presented for fiber orientation angles $\theta=(0^{\circ}, 30^{\circ}, 60^{\circ}, 90^{\circ})$. It can be observed that the maximum RMS displacement generally exhibits a positive correlation with the reduced

ISSN: 2688-8645

velocity. As the gas volume fraction increases, the maximum RMS displacements in the *X*, *Y*, and *Z* degrees of freedom further increase. At low reduced velocities ($U_r < 12$), the influence of fiber orientation angle is not pronounced; beyond this range, its effect becomes evident. Although the change in displacement amplitude remains modest, increasing the fiber orientation angle induces a downstream shift of the dominant vibration mode.

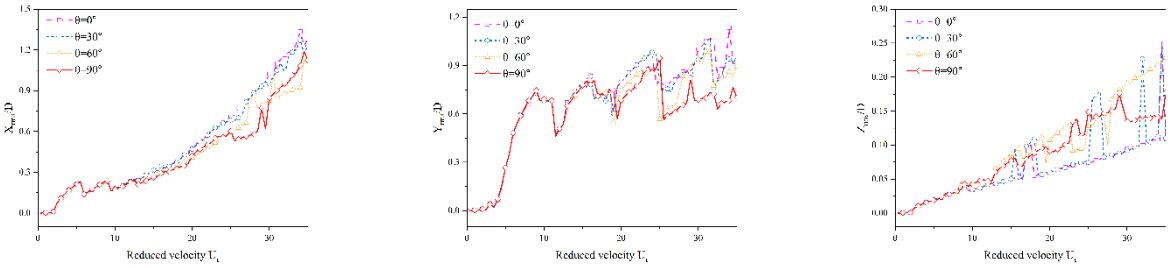

(a) *X* direction (b) *Y* direction (c) *Z* direction

Fig 7. Variation of the maximum RMS displacement with reduced velocity for different fiber orientation angles.

To investigate the effect of gas volume fraction on the vibration response, the system parameters are set according to Table 3, and gas volume fractions of 0, 0.3, 0.6, and 0.9 are considered. Fig. 8 presents the displacement time-history contour plots and the corresponding maximum-displacement envelopes for the catenary riser in the three degrees of freedom, while Fig. 9 shows the RMS displacement distributions along the riser.

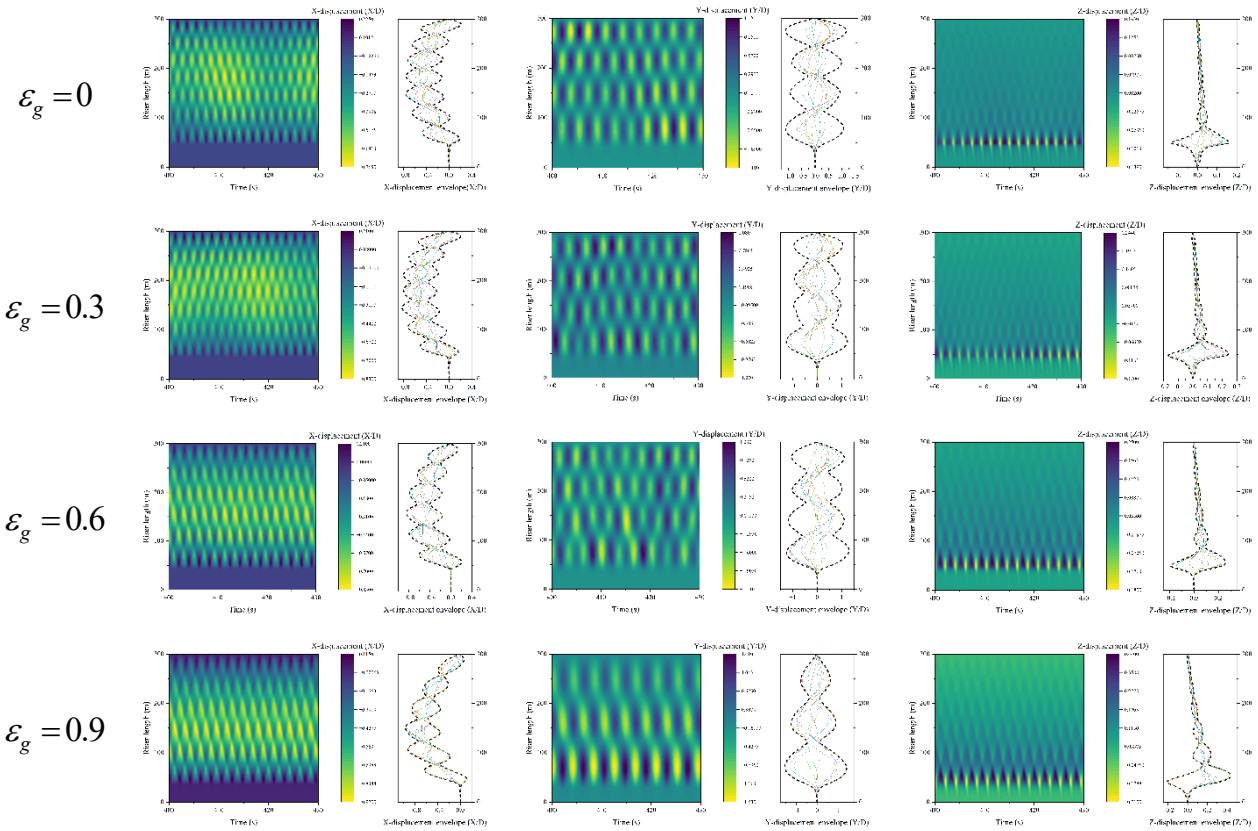

Fig 8. Displacement time-history contours and maximum-displacement envelopes for different gas volume fractions.

ISSN: 2688-8645

A displacement time-history contour plot visualizes the displacement magnitude at different times and spatial locations using a color scale, and is primarily used to illustrate how the structural deformation evolves over time. In Fig. 8, different colors correspond to different displacement levels; typically, cool colors (e.g., blue) indicate smaller displacements, while warm colors (e.g., red) represent larger displacements. It can be observed that the maximum displacement in the *X* direction is concentrated in the midspan region, the maximum displacement in the *Y* direction is more uniformly distributed along the riser, and the maximum displacement in the *Z* direction is concentrated in the touchdown region; a similar conclusion can also be drawn from Fig. 8. In the *X* and *Z* directions, the envelope curves become asymmetric due to the action of the external ocean current. Moreover, as the gas volume fraction ε_g increases from 0 to 0.9, the dominant vibration mode in the *X* and *Z* directions decreases from the 7th to the 6th order, while that in the *Y* direction decreases from the 4th to the 3rd order. As shown in Fig. 9, increasing the gas volume fraction ε_g from 0 to 0.9 leads to a pronounced increase in the RMS displacement in all three degrees of freedom, with the response mainly concentrated in the upstream portion of the riser.

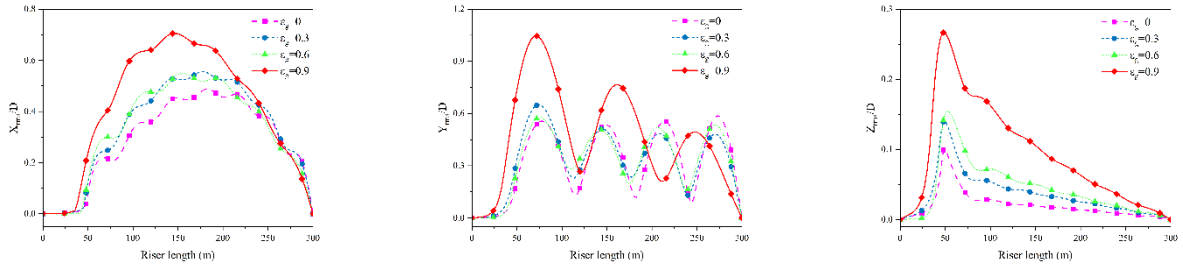

(a) RMS displacement in the X direction (b) RMS displacement in the Y direction (c) RMS displacement in the Z direction

Fig 9. RMS displacement distributions of the catenary riser for different gas volume fractions

To examine the influence of fiber orientation angle on the vibration response, the external current velocity is set to 0.3 m/s and the ply thickness is taken as 5 mm, while all other parameters follow Table 3. Fig. 10 presents the displacement time-history contour plots and the corresponding maximum-displacement envelopes for the catenary riser in the three degrees of freedom for fiber orientation angles of 0°, 30°, 60°, 90°. Fig. 11 shows the RMS displacement distributions along the riser for different fiber orientation angles.

As shown in Fig. 10, the maximum displacement in the *X* direction is concentrated in the midspan region, the maximum displacement in the *Y* direction is more uniformly distributed along the riser length, and the maximum displacement in the *Z* direction is concentrated in the touchdown region. In the *X* and *Z* directions, the envelope curves are asymmetric due to the action of the ocean current. Moreover, as the gas volume fraction ε_g increases from 0 to 0.9, the dominant vibration mode in the *X* and *Z* directions decreases from the 5th to the 4th order, while that in the *Y* direction decreases from the 3rd to the 2nd order. As shown in Fig. 11, consistent with the previous observations, the influence of fiber orientation angle is not significant for arc lengths below 50 m; beyond this point, its effect becomes evident. Although the change in displacement amplitude is relatively small, varying the fiber orientation angle induces a downstream shift of the dominant vibration mode.

ISSN: 2688-8645

4. Summary

This study investigates the mechanical behavior of a composite catenary riser subjected to the combined effects of internal gas–liquid flow and external ocean currents. The work consists of three main components—static modeling, dynamic modeling, and numerical solution—and systematically examines the mechanisms by which gas volume fraction and fiber orientation angle influence the static configuration and dynamic performance of the riser. The main conclusions are summarized as follows:

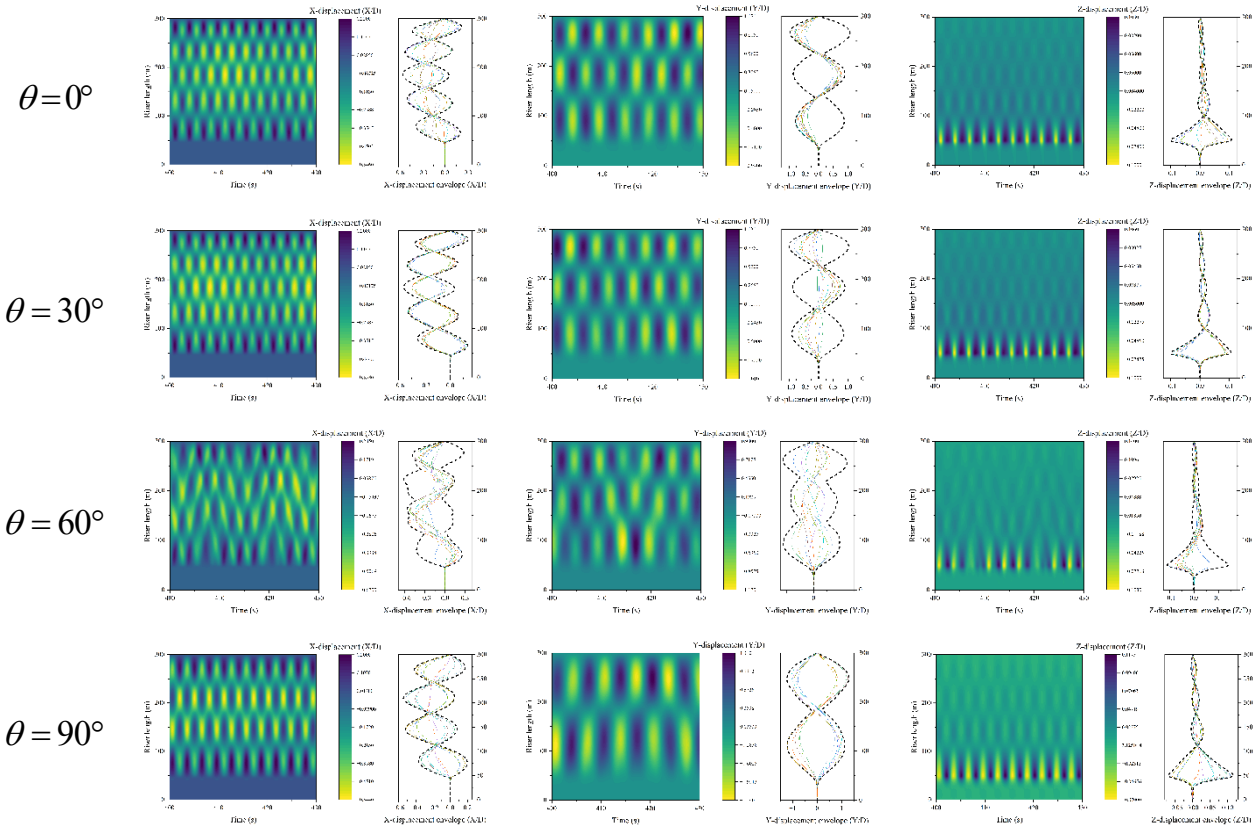

Fig 10. Displacement time-history contours and maximum-displacement envelopes for different fiber orientation angles

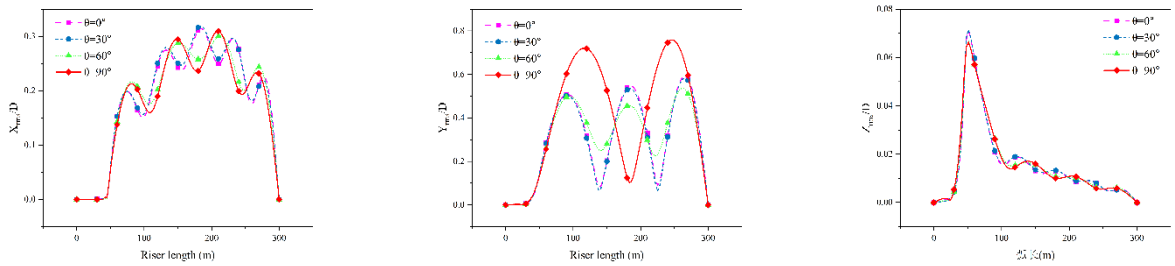

(a) RMS displacement in the X direction (b) RMS displacement in the Y direction (c) RMS displacement in the Z direction

Fig 11. RMS displacement distributions of the catenary riser for different fiber orientation angles.

(1) The gas volume fraction has a pronounced effect on the static configuration and internal forces of the composite catenary riser. Increasing the gas volume fraction effectively improves the static load state, reducing the tension, bending moment, and shear force in critical regions.

ISSN: 2688-8645

(2) By altering the coupling between axial and bending stiffness in the composite riser, the fiber orientation angle significantly affects the static equilibrium configuration and the distribution of internal forces. Smaller layup angles help improve the overall load state and reduce peak tension and bending moment in critical regions, whereas larger layup angles lead to a deeper sagging profile and increased local curvature and bending moment, which may exacerbate fatigue damage in the touchdown region.

(3) Increasing the gas volume fraction enlarges the displacement and vibration amplitude of the catenary riser and shifts the response toward lower-order vibration modes. By contrast, increasing the fiber orientation angle has a relatively minor effect on vibration amplitude, but it induces a downstream migration of the dominant vibration mode.

References

[1] Ochoa, O. O., Salama, M. M. Offshore composites: Transition barriers to an enabling technology. Composites Science and Technology. 2005, Vol. 65 (No. 15–16), p. 2588–2596.

[2] Chatjigeorgiou, I. K., Mavrakos, S. A. Nonlinear static analysis of deepwater catenary risers. Ocean Engineering. 2005, Vol. 32 (No. 1), p. 1–20.

[3] Sarpkaya, T. A critical review of the intrinsic nature of vortex-induced vibrations. Journal of Fluids and Structures. 2004, Vol. 19 (No. 4), p. 389–447.

[4] Kardomateas, G. A., Simitses, G. J. Buckling and postbuckling of composite cylindrical shells under external pressure. AIAA Journal. 1989, Vol. 27 (No. 11), p. 1522–1528.

[5] Facchinetti, M. L., de Langre, E., Biolley, F. Coupling of structure and wake oscillators in vortex-induced vibrations. Journal of Fluids and Structures. 2004, Vol. 19 (No. 2), p. 123–140.

[6] Monette, C., Pettigrew, M. J. Fluidelastic instability of flexible tubes subjected to two-phase internal flow. Journal of Fluids and Structures. 2004, Vol. 19 (No. 7), p. 943–956.

[7] Chang, X. P., Qu, C. J., Fan, J. M. Biaxially coupled vortex-induced vibration characteristics of composite marine risers conveying gas–liquid two-phase flow. Journal of Ocean University of China (Natural Science Edition). 2022, Vol. 52 (No. 10), p. 146–160. (in Chinese).

[8] Li, X., Cao, X., Li, F., et al. Coupled cross-flow/in-line vortex-induced vibration responses of a catenary-type riser subjected to uniform flows. Journal of Ocean University of China. 2024, Vol. 23 (No. 5), p. 1202–1212.

[9] Xing, H., Yu, Y., Xu, H., et al. Vortex-induced vibration response characteristics of catenary riser conveying two-phase internal flow. Ocean Engineering. 2022, Vol. 257, p. 111617.

[10] Chen, Y. B. Vortex-induced vibration and fatigue damage analysis of deepwater gas–liquid multiphase risers (PhD thesis, China Jiliang University, China 2016). (in Chinese).

[11] Li, H. J., Wang, J., Zhang, M. Research progress on vortex-induced vibration suppression technologies for marine risers. Ship Mechanics. 2020, Vol. 24 (No. 7), p. 935–949. (in Chinese).

[12] Tsukada, I. R., Morooka, K. C. A numerical procedure to calculate the VIV response of a catenary riser. Ocean Engineering. 2016, Vol. 122, p. 145–161.

[13] Yamamoto, C. T., Meneghini, J. R., Saltara, F., et al. Numerical simulations of vortex-induced vibration on flexible cylinders. Journal of Fluids and Structures. 2004, Vol. 19 (No. 4), p. 467–489.

[14] Liu, D. P., Ai, S. M., Sun, L. P., et al. Influence of steady slug flow on the dynamic response of steel catenary risers. Journal of Harbin Engineering University. 2021, Vol. 42 (No. 11), p. 1573–1579. (in Chinese).

[15] Liu, J., Guo, X. Q., Liu, Q. Y., et al. VIV response characteristics of marine risers considering coupled in-line and cross-flow vibrations. Acta Petrolei Sinica. 2019, Vol. 40 (No. 10), p. 1270–1282. (in Chinese).